# Statics and dynamics of electrowetting on pillar-arrayed surfaces at the nanoscale

Quanzi Yuan* and Ya-Pu Zhao*

The statics and dynamics of electrowetting on pillar-arrayed surfaces at the nanoscale are studied using molecular dynamics simulations. Under a gradually increased electric field, a droplet is pushed by the electromechanical force to spread, and goes through the Cassie state, the Cassie-to-Wenzel wetting transition and the Wenzel state, which can be characterized by the electrowetting number at the microscale $\eta_m$. The expansion of the liquid is direction-dependent and influenced by the surface topology. A positive voltage is induced in the bulk droplet, while a negative one is induced in the liquid confined among the pillars, which makes the liquid hard to spread and further polarize. Based on the molecular kinetic theory and the wetting states, theoretical models have been proposed to comprehend the physical mechanisms in the statics and dynamics of electrowetting, and are validated by our simulations. Our findings may help to understand the electrowetting on microtextured surfaces and assist the future design of engineered surfaces in practical applications.
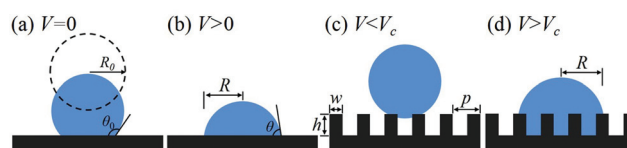
## 1. Introduction

Electrowetting is a powerful tool in manipulating small droplets.[1–5] Owing to a variety of micro/nanofluidic applications, such as lab-on-chip,[6] energy harvesting,[7] optofluidics,[8] biomedical devices[9] *etc.*, electrowetting has received significant research attention in the past decade.

At the macroscale, an external applied voltage $V$ reduces the contact angle of a liquid droplet on a smooth solid (Fig. 1b).[10,11] In the usual electrowetting setup, a pure water droplet with an ion concentration of $10^{-7}$ M spreads when $V \sim 10$ V.[12] The external electric field is screened in the double layer, whose thickness is the Debye screening length $D \sim 1$ μm, at the solid–liquid interface. The apparent contact angle $\theta$ decreases from an initial contact angle $\theta_0$ and can be described by the Lippmann–Young equation:

$$\cos \theta = \cos \theta_0 + \eta, \quad (1)$$

where $\eta = CV^2/2\gamma_{LV} < 1$, $C = \varepsilon\varepsilon_0/d$, $\varepsilon_0$, $\varepsilon$, $d$ and $\gamma_{LV}$ are the electrowetting number, the capacitance per unit area, the vacuum permittivity, the relative permittivity, and the distance between the electrodes and liquid–vapour interface energy, respectively.[13,14] With the trend of miniaturization, more attention has been drawn to smaller scales. At the microscale, the size of a water droplet is smaller than $D$. The electric field permeates

*State Key Laboratory of Nonlinear Mechanics, Institute of Mechanics, Chinese Academy of Sciences, Beijing 100190, People's Republic of China. E-mail: yzhao@imech.ac.cn, yuanquanzi@lnm.imech.ac.cn*

**Fig. 1** Illustration of (a) a droplet of initial radius $R_0$ on a smooth solid with an equilibrium contact angle of $\theta_0$, and (b) a droplet electrowets on a smooth solid with contact angle $\theta < \theta_0$. (c) The Cassie state of a droplet on a pillar-arrayed surface when voltage $V$ is less than the critical voltage $V_c$. (d) The Wenzel state of a droplet on a pillar-arrayed surface when voltage $V$ is larger than the critical voltage $V_c$. $p$, $w$ and $h$ are the period, width and height of the pillars, respectively. $R$ is the radius of the liquid.

the whole droplet, although the water is polarized to screen the external field, especially at the interface.[15] The electric interaction is $-\sum_i |E||\mu_i|L(|E||\mu_i|/k_B T)$ and could be simplified as $-\sum_i |E|^2|\mu_i|^2/k_B^i T$ in a weak field, where $E$, $\mu$, $k_B$, $T$ and $L(x)$ are the electric field vector, water dipole vector, Boltzmann constant, absolute temperature and Langevin function, respectively.[16] Thus, the governing equation is the same as that at the macroscale if we define an electrowetting number at the microscale $\eta_m = C_m V^2/2\gamma_{LV}$, where $C_m$ is the effective capacitance per unit area.

When a droplet electrowets on a rough surface, the situation becomes complicated.[17,18] Under a weak voltage, the droplet is in the Cassie state, and sits on a composite surface of vapour and solid (Fig. 1c).[19] With the increase in voltage, the electromechanical force, *i.e.* the Maxwell force, pulls the liquid to spread it and decreases the contact angle.

A Cassie-to-Wenzel wetting transition does not happen until the applied voltage exceeds a critical value $V_c$.[20] The confined vapour cannot sustain the above liquid, and therefore suddenly breaks down.[21] Meanwhile, the droplet impales into the pillars. Under a high voltage, the droplet is in the Wenzel state, in close contact with the solid (Fig. 1d). Dai and Zhao developed an extended electrowetting equation for rough surfaces to predict the change of the contact angle under the electric field.[22] However, the statics and dynamics of electrowetting on rough surfaces are still far from well-understood, especially at the nanoscale.

In this paper, a molecular picture of the electrowetting on pillar-arrayed surfaces at the nanoscale is first provided using molecular dynamics (MD) simulations. The statics and dynamics of electrowetting on pillar-arrayed surfaces are explored at the atomic level and compared with those on smooth surfaces. With the increase of the external applied voltage, the droplet goes through the Cassie state, the Cassie-to-Wenzel transition and the Wenzel state, which is closely related to the surface topology and the electrowetting number at the microscale $\eta_m$. The critical voltage, which could trigger the Cassie-to-Wenzel wetting transition, and its relation to the surface roughness are also analysed. The electrowetting on pillar-arrayed surfaces is found to be direction-dependent. The polarized liquid is confined in the pillars, making the liquid hard to spread and further polarize. Further, theoretical models are proposed to understand the physical mechanisms in the statics and dynamics of electrowetting, and are validated by our simulations. Our findings may help to understand the electrowetting on microtextured surfaces and assist the future design of engineered surfaces in practical applications.

## 2. Model and methods

Large scale MD simulations implemented in LAMMPS[23] were carried out to explore the dynamics and phase transition of electrowetting of a droplet on smooth and pillar-arrayed surfaces at the atomic level. The simulation domain was composed of a smooth or pillar-arrayed hydrophobic solid surface and a water droplet (radius $R_0 = 3$ nm), as shown in Fig. 2. Topological parameters [$w$, $h$, $p$], surface roughness $ro$ and density of roughness $\phi_s$ of these samples were varied and are listed in Table 1.

The surface roughness is defined as the ratio between the actual and projected surface areas and $ro = 1 + 4\,wh/p^2$ for square pillars. The larger the $ro$ is, the larger is the actual surface area. The density of roughness is defined as the ratio of the area of the top faces to the total base area and $\phi_s = w^2/p^2$ for square pillars. Because the pillar heights of all the samples are the same, the smaller the $\phi_s$ is, the larger is the space among the pillars. The solid atoms were fixed during the simulations.[24] The droplet was modelled using the extended simple point charge (SPC/E) water model[25,26] with viscosity $\mu = 0.729$ mPa s, density $\rho = 994$ kg m$^{-3}$, and surface energy $\gamma_{LV} = 0.0636$ N m$^{-1}$, which are close to those of real water. The water
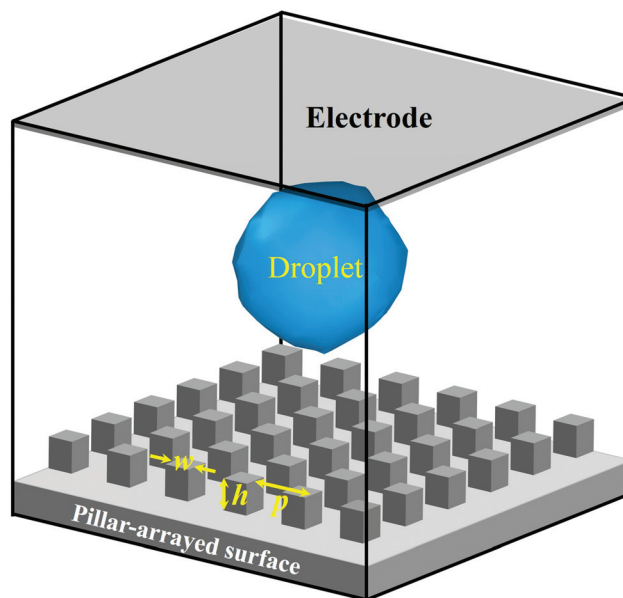


**Fig. 2** The simulation domain. From top to bottom: The top grey layer is the electrode in electrowetting. The blue sphere is the water droplet. The grey substrate is the pillar-arrayed hydrophobic solid surface. The pillar width $w$, the pillar height $h$ and the period of the array $p$ are labelled on the pillars.

**Table 1** Topological parameters of the smooth and pillar-arrayed surfaces

| Sample | $w$ (nm) | $h$ (nm) | $p$ (nm) | $ro$ | $\phi_s$ |
|--------|----------|----------|----------|------|----------|
| 1 | 0.000 | 0.000 | 0.000 | 1.000 | 0.000 |
| 2 | 1.020 | 1.224 | 3.468 | 1.415 | 0.086 |
| 3 | 1.020 | 1.224 | 3.060 | 1.533 | 0.111 |
| 4 | 1.020 | 1.224 | 2.652 | 1.710 | 0.148 |
| 5 | 1.020 | 1.224 | 2.244 | 1.992 | 0.207 |
| 6 | 1.020 | 1.224 | 1.836 | 2.482 | 0.309 |

droplet is modelled as a polar fluid and is not conductive. The total potential energy $E_{ij}$ between two atoms i and j separated by $r_{ij}$ is the sum of the Lennard–Jones potential plus the Coulombic pairwise interaction

$$E_{ij} = 4\varepsilon_{ij}\left[\left(\frac{\sigma_{ij}}{r_{ij}}\right)^{12} - \left(\frac{\sigma_{ij}}{r_{ij}}\right)^6\right] + k_e\frac{q_iq_j}{r_{ij}}, \qquad (2)$$

where $\varepsilon$ is the depth of the potential well, $\sigma$ is the zero-crossing distance for the potential, $k_e = 8.988 \times 10^9$ N m$^2$ C$^{-2}$ is the Coulomb constant and $q$ is the charge on the atom.

First, a water droplet was placed on an uncharged solid surface to achieve an equilibrium state, as shown in Fig. 1 and 2. Then, two surfaces with a cross-sectional area of $A$ separated by a distance $d$ were charged to imitate the usual setup of electrowetting. The top layer of the solid surface was charged with $Q$, whilst the layer at the top of the simulation domain was charged with $-Q$. Therefore, the applied electric field $E$ and voltage $V$ can be calculated as $E = Q/(A\varepsilon_0\varepsilon_w)$ and $V = Qd/(A\varepsilon_0\varepsilon_w)$, where $\varepsilon_0$ and $\varepsilon_w$ are the vacuum permittivity and the relative

permittivity of water, respectively. $E \sim 1$ V nm$^{-1}$ and $V \sim 10$ V, which are the typical values for pure water in the electrowetting setup. Generally, the contact angle of a water droplet is used to characterize the wettability of a solid surface.[27] When an external voltage $V$ is applied, a droplet electrowets the hydrophobic solid surface and its contact angle decreases with the increase of $V$. Therefore, the apparent wettability of the solid surface increases with the increase of $V$. The simulation time and time step were carefully selected so as to take fully into account the behaviour of the droplet and the atomic details.

## 3.  Results and discussion

### 3.1  Statics of electrowetting on rough surfaces

The electrowetting of a water droplet on a smooth solid was carried out as shown in Fig. 3a. When there was no external voltage, the droplet wetted the hydrophobic surface with an equilibrium contact angle $\theta_0 = 125°$ (0.0 V, Fig. 3a). With an increase in the voltage, the wettability of the solid increased. A precursor film, *i.e.* a thin molecular film, advanced ahead of the nominal contact line.[28] Driven by the electric energy, the bulk droplet spread on the top of the precursor film. However, water did not completely wet the precursor film.[29] What is more, the precursor film showed a hydrophobic feature to the above bulk droplet under a weak voltage (6.2 V, Fig. 3a), because of the ice-like and two-dimensional hydrogen-bond network in the precursor film.[28] Further increase of the voltage resulted in stronger polarization of the water at the interface, making the contact angle $\theta$ smaller than 90° (12.4 V, Fig. 3a). When $V \geq 18.6$ V, the liquid completely wetted the solid and became a liquid film. The variation of energy with the square of the applied voltage $V^2$, whose slope represents the capacitance of the system, is plotted using black squares in Fig. 4.

The electrowetting of a water droplet on the pillar-arrayed surfaces was simulated as shown in Fig. 3b–d. Taking Fig. 3c as an example, typically the droplet went through two stages. In the first stage, the droplet was deposited on the pillars with a confined vapour layer filling the gap among the pillars. The apparent contact angle $\theta_a$ of the water droplet on the pillars with $ro = 1.710$ was about 140° when there was no external
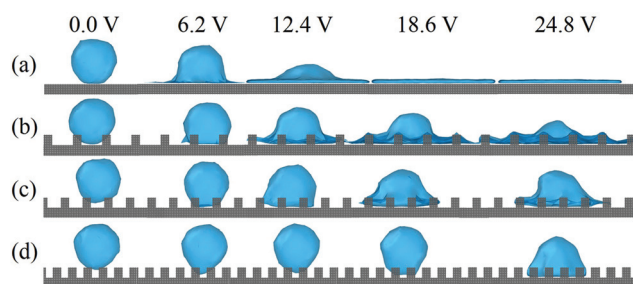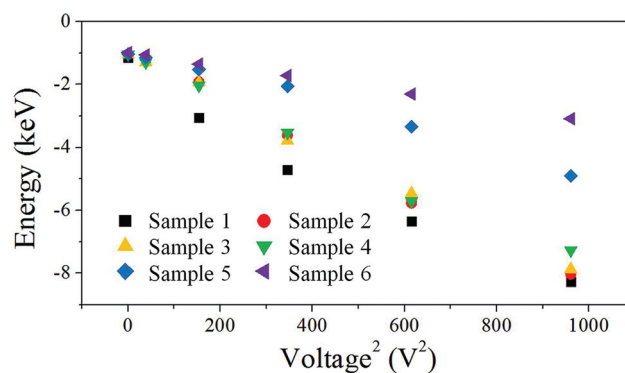


**Fig. 4** Variation of the equilibrium energy of the system with respect to square of the applied voltage. The symbols represent samples with different surface roughnesses.

electric field. Under a weak voltage, the droplet remained in the Cassie state (<6.2 V, Fig. 3c). Driven by the electromechanical force, the liquid tended to wet the surface of the pillars, and the air pocket was compressed simultaneously. $\theta_a$ could be obtained by considering both the Cassie–Baxter relation[30] $\cos\theta = \phi_s(\cos\theta_0 + 1) - 1$ and eqn (1):
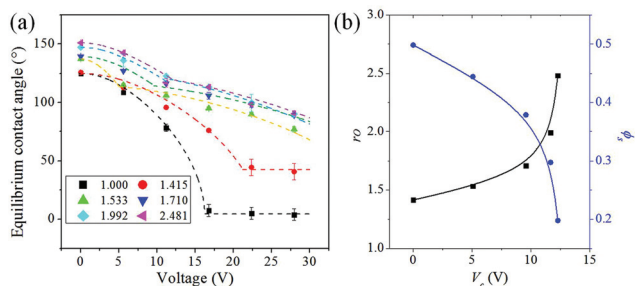
$$\cos\theta_a = \phi_s(\cos\theta_0 + \eta_m + 1) - 1. \tag{3}$$

With further increase in voltage, the Cassie-to-Wenzel transition took place: the air pocket collapsed and the droplet impaled into the pillars to change into the Wenzel state. In the second stage, $\theta_a$ could be obtained by considering both the Wenzel relation[31] $\cos\theta = ro\cos\theta_0$ and eqn (1):

$$\cos\theta_a = ro(\cos\theta_0 + \eta_m). \tag{4}$$

The first stage was not necessary for surfaces with small $ro$. In Fig. 3b, the wetting transition happened instantly when the droplet was deposited on the pillars. The droplet was pulled by the pillars to be in close contact with the solid and directly went into the second stage. For surfaces with small $ro$ and large $\phi_s$, the pinning force from the pillars to the liquid is small and the expansion was easy in electrowetting (Fig. 3b). For surfaces with large $ro$, the liquid was pinned by the pillars and the droplet was hard to expand (Fig. 3d). As shown in Fig. 4, the energy decreased almost linearly with the increase of $V^2$. The larger the surface roughness was, the smaller was the capacitance of the system. The reason was because the surface roughness increased the average distance between the electrode and the liquid.

The variation of $\theta_a$ with respect to $V$ was quantitatively recorded in Fig. 5a. When the droplet electrowetted on a smooth surface (black squares), $\theta_a$ decreased with the increase of $V$, which obeyed eqn (1) (the Lippmann–Young equation) shown in the black dashed line. When $\theta_a$ reached zero, the electrowetting was saturated and $\theta_a$ could no longer decrease. When the droplet electrowetted on a pillar-arrayed surface, the decrease of $\theta_a$ was slower than that on a smooth surface. For small $ro = 1.415$, the droplet was initially in the Wenzel state. So $\theta_a$ decreased as described in eqn (4) until it reached a



**Fig. 3** Equilibrium configurations of a water droplet electrowetting on (a) a smooth surface, and pillar-arrayed surfaces with (b) $ro = 1.415$, (c) $ro = 1.710$ and (d) $ro = 2.482$ under different voltages.

**Fig. 5** (a) Variation of the apparent contact angle with respect to the applied voltage. The symbols represent samples with different surface roughnesses. (b) Variation of the critical voltage $V_c$ with respect to the surface roughness $ro$ (black squares) and the density of roughness $\phi_s$ (blue circles). The critical voltage $V_c$ is defined as the voltage when the Cassie-to-Wenzel wetting transition happens.

saturated value $\theta_s \approx 42.64°$. For large $ro$, the droplet changed from the Cassie state to the Wenzel state. So there existed a turning point of $\theta_a$, which corresponded to the critical voltage $V_c$ when wetting transition happened. Eqn (3) was used to fit the variation of $\theta_a$ before $V_c$, while eqn (4) was used to fit $\theta_a$ after $V_c$, which are represented by the dashed lines in Fig. 5a. $V_c$ was found to increase with the increase of $ro$ and $\phi_s$ (Fig. 5b). With larger $ro$ or $\phi_s$, the distance $(p - w)$ between two adjacent pillars is shorter. According to the Young–Laplace equation, a larger pressure is needed to overcome the Laplace pressure $P = 2\gamma_{LV}/(p - w)$. Therefore, a larger critical voltage $V_c$ is necessary.

The electrowetting on pillar-arrayed surfaces depends on the wetting directions. There exist fast and slow directions for the electrowetting, which varies with the applied voltage. Fig. 6 is plotted in polar coordinates, in which the radial coordinate represents the voltage, the angular coordinate represents the direction and the colour represents the distance between the origin and the liquid front labelled by the colour legend. The
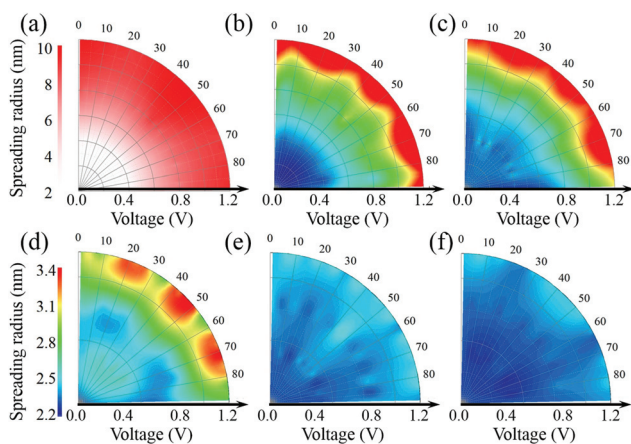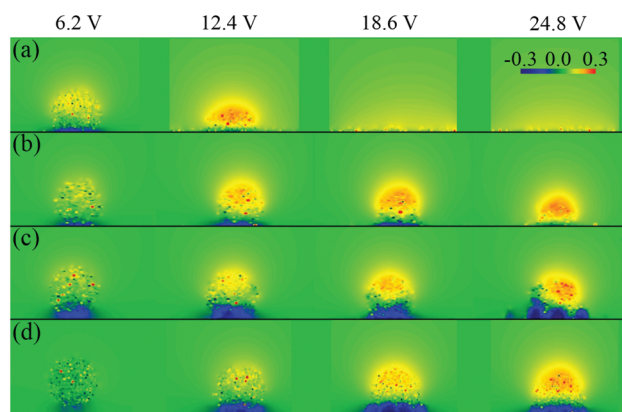
electrowetting on a smooth solid was isotropic, as shown in Fig. 6a. With the increase of the voltage, the projection of the droplet gradually expanded in the shape of nearly a circle.

In contrast, the electrowetting on a pillar-arrayed surface was anisotropic, *i.e.* the liquid radius depended on the spreading directions, as shown in Fig. 6b–f. The liquid propagated ahead of the bulk among the charged pillars. The charged pillars drive the liquid to electrowet, while it dissipates energy for the liquid to spread from one pillar to another. The distance between the pillars varied with the flow direction. The electrostatic force is inversely proportional to the distance and the net charge on each pillar is the same. Hence, when the distance between two pillars is shorter in a direction, the driving force is large, making the liquid electrowet faster. Therefore, the spreading radius on a pillar-arrayed surface depends on the direction. Furthermore, the velocity was symmetric about the orthogonal and diagonal directions because of the arrangement of the pillars.[32] Taking Fig. 6c as an example, when $V = 6$ V, the liquid radius spread slower along 0°, 45° and 90°, and faster along 22.5° and 67.5°. When $V = 12$ V, the fast and slow directions changed: the liquid radius spread slower along 0°, 35°, 65° and 90°, and faster along 20°, 45° and 70°. By comparing Fig. 6, we found the fast and slow directions depend on the surface roughness and the voltage. The overall color of Fig. 6b–f gradually changed from red to blue, which implies that the liquid radius decreased with the increase of the surface roughness under a certain voltage.

The water molecules, especially at the interface, are polarized when an external voltage is applied. The electric field formed by the polarized liquid counteracts the effect of the external field,[33] and the induced local voltage together with the confinement of the pillars may be the reason for saturation in electrowetting on rough surfaces. When a droplet electrowetted on a smooth solid, the induced positive voltage was mainly located in the bulk droplet, while the negative voltage concentrated in the precursor film, as shown in Fig. 7a.



**Fig. 6** Spreading radius in different directions with respect to the applied voltage for (a–f) samples 1–6. The origin $O$ is put in the center of the droplet. The two colour legends are for (a) and (b–f), respectively. The radial coordinate represents the voltage, the angular coordinate represents the direction and the colour represents the spreading radius.



**Fig. 7** The local voltage distribution caused by the water droplet on (a) a smooth surface and on pillar-arrayed surfaces with (b) $ro = 1.415$, (c) $ro = 1.710$ and (d) $ro = 2.482$, under different external voltages. The color represents the local voltage. The bottom of each figure is the solid surface and the top is the top electrode, as shown in Fig. 2.

Hence, the bulk droplet and the precursor film formed a dipole to screen the external electric field. With the increase of the external voltage (12.4 V), the voltage of the spherical cap became larger, and so did the bottom layer, which could be reflected by the change in color. When the external voltage was increased to 18.6 V, the bulk droplet vanished and there was only a liquid layer, which means that the liquid completely wetted the solid surface, as shown in Fig. 3a. On further increasing the voltage (24.8 V), the liquid could not be further polarized.

The situation was different on pillar-arrayed surfaces (Fig. 7b–d). The induced positive voltage was still located in the bulk, while the negative voltage was mainly confined among the pillars. Because of the excess surface area of the pillars, the external electric field increased the affinity of the water molecules in the forest of pillars. The pillars were charged with positive $Q$, and the liquid with negative voltage was confined among the pillars and attracted by the pillars. It dissipated more energy to push the water confined in the pillars. The attractive interaction between the liquid and the pillars blocked the further spreading of the liquid. The denser the pillars are, the stronger are the confinement and attraction of the pillars to the liquid. When $ro$ is small, the blue part became smaller with the increase of the external voltage, which implied that the negative part of the dipole gradually spread among the pillars. However, the apparent contact angle saturated at about 42.64° as shown in Fig. 5a. When $ro$ was large, the blue part expanded but did not become smaller, which meant that it was hard to drive the negative part of the dipole to spread even under a high external voltage. Because of the confinement of the pillars, the induced negative voltage blocked the further decrease of the apparent contact angle. The introduction of new length scales might be the reason for saturation in electrowetting on a rough surface.[34]

## 3.2. Dynamics of electrowetting on rough surfaces

In the dynamic wetting process, the liquid wets the solid with the capillary velocity $U_{CA} = \gamma_{LV}/\mu$. In the electrowetting process, the liquid spreads on the solid with a characteristic speed of $U_{EL} = \eta_m U_{CA} = C_m V^2/2\mu$. Because $\eta_m < 1$, $U_{EL} < U_{CA} \sim 10^2$ m s$^{-1}$. We quantitatively recorded the evolution of the spreading radius $R$ with respect to time in our MD simulations, as shown in Fig. 8.

For the smooth surface, $R$ expanded smoothly and tended to an equilibrium value (Fig. 8a). If we use the power law $R \sim t^n$ to fit these curves, the scaling exponent $n$ increased with the external voltage $V$.[28] For the pillar-arrayed surfaces, there existed a sharp transition in the $R$–$t$ curves because of surface topology and the Cassie-to-Wenzel transition. In the case of Fig. 8b, the droplet stayed in the Wenzel state on the surface with $ro = 1.415$. In the case of Fig. 8d, the droplet was initially in the Cassie state and changed into the Wenzel state when $V$ exceeded $V_c$. The complex interactions between the pillars and the liquid made the evolution of $R$ on pillar-arrayed surfaces seem arbitrary. However, the dynamics of the liquid obeyed rules, depending on the wetting state.
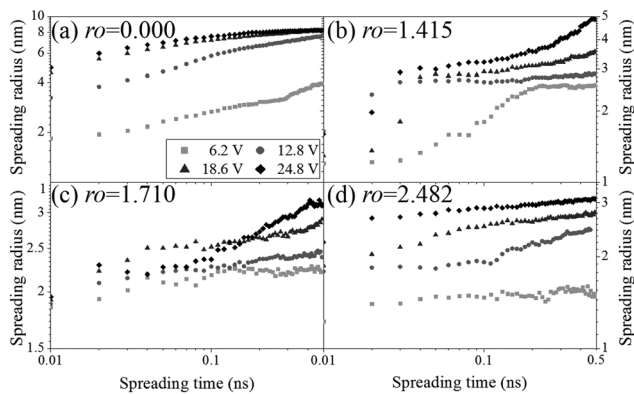


Fig. 8 MD results of the evolution of the spreading radius with respect to time for droplet electrowetting on (a) a smooth surface, and on pillar-arrayed surfaces with (b) $ro$ = 1.415, (c) $ro$ = 1.710 and (d) $ro$ = 2.482. The squares, circles, triangles and diamonds represent data under an external voltage $V$ = 6.2, 12.4, 18.6 and 24.8 V, respectively.

For instance, we adopted the molecular kinetic theory (MKT), which was proposed by Eyring et al.,[35] to analyze the dynamics of electrowetting. For the water molecules that jump between gold surface sites separated by a distance $\lambda$ with an equilibrium frequency $\kappa_0 = (k_B T/\mu \nu_m)\exp(-\lambda^2 Wa/k_B T)$, the advancing velocity $U = 2\kappa_0 \lambda \sinh(F\lambda^2/2k_B T)$, driven by the driving work per unit area $F$, where $k_B$, $T$, $\nu_m$, $\mu$ and $Wa$ are the Boltzmann constant, absolute temperature, molecular flow volume, fluid viscosity and work of adhesion between the solid and the liquid, respectively. In our case, the ratio of the driving work $F\lambda^2$ to the thermal energy $k_B T$ is of the order of 0.1 to 1. Therefore, $\sinh(F\lambda^2/2k_B T) \approx F\lambda^2/2k_B T$ could be a good approximation. We could simplify the governing equation of the liquid:

$$U = \frac{F\lambda^3}{\mu \nu_m} \exp\left(-\frac{\lambda^2 Wa}{k_B T}\right). \tag{5}$$

Once the liquid–solid pair and the topology of the substrate are fixed, $\mu$, $\lambda$, $\nu_m$ and $Wa$ are all constant, $U = C_1 F/\mu$, where $C_1 = (\lambda^3/\nu_m)\exp(-\lambda^2 Wa/k_B T)$ is a constant of the order of $10^{-4}$–$10^{-1}$.

When a droplet electrowets on a smooth surface, $F = \gamma_{LV}(\cos\theta_0 + \eta_m - \cos\theta)$, the governing equation is obtained from eqn (5):

$$U = \dot{R} = C_1 \frac{\gamma_{LV}}{\mu}\left(\cos\theta_0 + \frac{C_m V^2}{2\gamma_{LV}} - \cos\theta\right), \tag{6}$$

where $U_{CA} = \gamma_{LV}/\mu$ is the capillary velocity. In our models, the evaporation is not taken into consideration, so the total mass (or volume) of the droplet does not change. Taking into account the geometry of the droplet $\theta = \theta(R)$ and substituting into eqn (6), we can achieve the dynamics of electrowetting on a smooth solid.

When a droplet electrowets on a pillar-arrayed surface, the governing equations for the Cassie and Wenzel state are distinguished. If the droplet sits on the air pocket and the pillar
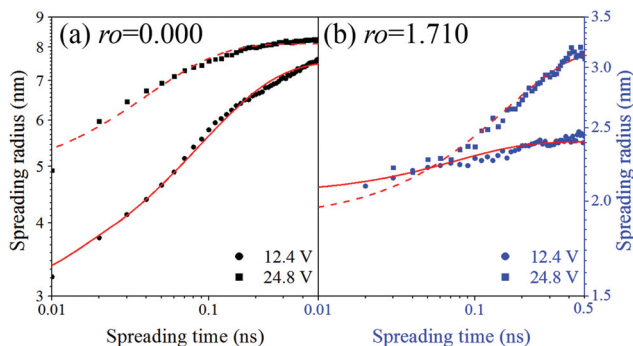
**Fig. 9** The evolution of the spreading radius with respect to time for droplets on (a) a smooth surface, and (b) a pillar-arrayed surface with *ro* = 1.710. The circles and squares represent MD results when external voltage *V* = 12.4 and 24.8 V, respectively. The dashed and solid lines represent theoretical predictions when external voltage *V* = 12.4 and 24.8 V, respectively.

tops, $F = \gamma_{LV}[\phi_s(\cos\theta_0 + \eta_m + 1) - 1 - \cos\theta]$, the governing equation of the Cassie state is

$$U = \dot{R} = C_1 \frac{\gamma_{LV}}{\mu}\left[\phi_s\left(\cos\theta_0 + \frac{C_m V^2}{2\gamma_{LV}} + 1\right) - 1 - \cos\theta\right]. \quad (7)$$

If the liquid penetrates into the pillars and is in close contact with the solid, $F = \gamma_{LV}[ro(\cos\theta_0 + \eta_m) - \cos\theta]$, the governing equation of the Wenzel state is

$$U = \dot{R} = C_1 \frac{\gamma_{LV}}{\mu}\left[ro\left(\cos\theta_0 + \frac{C_m V^2}{2\gamma_{LV}}\right) - \cos\theta\right] \quad (8)$$

Taking into account the geometry of the droplet $\theta = \theta(R)$ and substituting into eqn (7) and (8), we can obtain the dynamics of electrowetting on pillar-arrayed surfaces.

Taking into account the physical quantities used in our simulations, we numerically solved eqn (6) for smooth surfaces and eqn (7) and (8) for rough surfaces, respectively, and the evolution of the spreading radius with respect to time was obtained, as shown in Fig. 9. The theoretical predictions fitted well with the MD results.

## 4. Conclusions

In this article, MD simulations and theoretical approaches are employed to explore the statics and dynamics of droplet electrowetting on pillar-arrayed surfaces at the nanoscale. The electrowetting number at the microscale $\eta_m = C_m V^2/2\gamma_{LV}$ is important in characterizing the electrowetting state. When there is no external electric field, the droplet is in the Cassie state. When an external electric field is applied, electromechanical force increases with the increase of the voltage to push the droplet towards the solid and pull the liquid to spread. The Cassie-to-Wenzel wetting transition takes place and the droplet suddenly changes to the Wenzel state as long as the voltage exceeds a critical value. We also found that the expansion of liquid depends on its direction because of the arrangement of the pillars. The external field induces a positive voltage in the bulk droplet and a negative one confined in the pillars, which makes the liquid hard to spread and further polarize. We have proposed theoretical models to comprehend the physical mechanisms in the statics and dynamics of electrowetting, which are validated by our simulations. Our findings may help to understand the electrowetting on micro-textured surfaces and assist the future design of engineered surfaces in practical applications.

## Acknowledgements

## Notes and references

1 W. J. Welters and L. G. Fokkink, *Langmuir*, 1998, **14**, 1535–1538.
2 M. G. Pollack, R. B. Fair and A. D. Shenderov, *Appl. Phys. Lett.*, 2000, **77**, 1725–1726.
3 T. B. Jones, *Langmuir*, 2002, **18**, 4437–4443.
4 S. K. Cho, H. Moon and C.-J. Kim, *J. Microelectromech. Syst.*, 2003, **12**, 70–80.
5 Y. P. Zhao, *Theor. Appl. Mech. Lett.*, 2014, **4**, 034002.
6 S.-K. Fan, P.-W. Huang, T.-T. Wang and Y.-H. Peng, *Lab Chip*, 2008, **8**, 1325–1331.
7 T. Krupenkin and J. A. Taylor, *Nat. Commun.*, 2011, **2**, 448.
8 D. Psaltis, S. R. Quake and C. Yang, *Nature*, 2006, **442**, 381–386.
9 J. T. Feng and Y. P. Zhao, *Biomed. Microdevices*, 2008, **10**, 65–72.
10 C. Quilliet and B. Berge, *Curr. Opin. Colloid Interface Sci.*, 2001, **6**, 34–39.
11 F. Mugele and J. Baret, *J. Phys.: Condens. Matter*, 2005, **17**, R705–R774.
12 J. Berthier, *Micro-drops and digital microfluidics*, William Andrew, 2012.
13 G. Lippmann, *Ann. Chim. Phys.*, 1875, **5**, 494–549.
14 Y. Wang and Y. P. Zhao, *Soft Matter*, 2012, **8**, 2599–2606.
15 V. Ballenegger and J.-P. Hansen, *J. Chem. Phys.*, 2005, **122**, 114711.
16 C. D. Daub, D. Bratko, K. Leung and A. Luzar, *J. Phys. Chem. C*, 2007, **111**, 505–509.
17 D. L. Herbertson, C. R. Evans, N. J. Shirtcliffe, G. McHale and M. I. Newton, *Sens. Actuators, A*, 2006, **130**, 189–193.
18 V. Bahadur and S. V. Garimella, *Langmuir*, 2007, **23**, 4918–4924.
19 T. Koishi, K. Yasuoka, S. Fujikawa, T. Ebisuzaki and X. C. Zeng, *Proc. Natl. Acad. Sci. U. S. A.*, 2009, **106**, 8435.

20 G. Manukyan, J. Oh, D. Van Den Ende, R. Lammertink and F. Mugele, *Phys. Rev. Lett.*, 2011, **106**, 014501.

21 P. Papadopoulos, L. Mammen, X. Deng, D. Vollmer and H.-J. Butt, *Proc. Natl. Acad. Sci. U. S. A.*, 2013, **110**, 3254–3258.

22 W. Dai and Y. P. Zhao, *J. Adhes. Sci. Technol.*, 2008, **22**, 217–229.

23 S. Plimpton, *J. Comput. Phys.*, 1995, **117**, 1–19.

24 T. Koishi, K. Yasuoka, T. Ebisuzaki, S. Yoo and X. C. Zeng, *J. Chem. Phys.*, 2005, **123**, 204707.

25 M. A. González and J. L. F. Abascal, *J. Chem. Phys.*, 2010, **132**, 096101.

26 C. Vega and E. de Miguel, *J. Chem. Phys.*, 2007, **126**, 154707.

27 A. Marmur, *Annu. Rev. Mater. Res.*, 2009, **39**, 473–489.

28 Q. Z. Yuan and Y. P. Zhao, *Phys. Rev. Lett.*, 2010, **104**, 246101.

29 C. Wang, H. Lu, Z. Wang, P. Xiu, B. Zhou, G. Zuo, R. Wan, J. Hu and H. P. Fang, *Phys. Rev. Lett.*, 2009, **103**, 137801.

30 A. Cassie and S. Baxter, *Trans. Faraday Soc.*, 1944, **40**, 546–551.

31 R. N. Wenzel, *Ind. Eng. Chem.*, 1936, **28**, 988–994.

32 Q. Z. Yuan and Y. P. Zhao, *J. Fluid Mech.*, 2013, **716**, 171–188.

33 Z. Sun, D. Pan, L. Xu and E. Wang, *Proc. Natl. Acad. Sci. U. S. A.*, 2012, **109**, 13177–13181.

34 J. Liu, M. Wang, S. Chen and M. O. Robbins, *Phys. Rev. Lett.*, 2012, **108**, 216101.

35 S. Glasstone, K. Laidler and H. Eyring, *The Theory of Rate Processes*, McGraw-Hill, New York, 1941.